AGU PUBLICATIONS

JGR

Journal of Geophysical Research: Earth Surface

RESEARCH ARTICLE
10.1002/2015JF003791

Coupled ice shelf-ocean modeling and complex grounding line retreat from a seabed ridge

J. De Rydt[1] and G. H. Gudmundsson[1]

[1] British Antarctic Survey, Cambridge, UK

Key Points:
- New offline coupled ice shelf-ocean model is developed and tested for Pine Island-like geometry
- Ocean-driven retreat of Pine Island Glacier from a seabed ridge becomes irreversible after 20 years
- Simple melt rate parameterization overestimates mass loss by 40% compared to coupled simulations

Supporting Information:
- Supporting Information S1
- Movie S1
- Movie S2

Correspondence to:
J. De Rydt,
janryd69@bas.ac.uk

Citation:
De Rydt, J., and G. H. Gudmundsson (2016), Coupled ice shelf-ocean modeling and complex grounding line retreat from a seabed ridge, *J. Geophys. Res. Earth Surf.*, *121*, 865–880, doi:10.1002/2015JF003791.

Received 13 NOV 2015
Accepted 23 MAR 2016
Accepted article online 28 MAR 2016
Published online 4 MAY 2016

Abstract Recent observations and modeling work have shown a complex mechanical coupling between Antarctica's floating ice shelves and the adjacent grounded ice sheet. A prime example is Pine Island Glacier, West Antarctica, which has a strong negative mass balance caused by a recent increase in ocean-induced melting of its ice shelf. The mass loss coincides with the retreat of the grounding line from a seabed ridge, on which it was at least partly grounded until the 1970s. At present, it is unclear what has caused the onset of this retreat and how feedback mechanisms between the ocean and ice shelf geometry have influenced the ice dynamics. To address these questions, we present the first results from an offline coupling between a state-of-the-art shallow-ice flow model with grounding line resolving capabilities and a three-dimensional ocean general circulation model with a static implementation of the ice shelf. A series of idealized experiments simulate the retreat from a seabed ridge in response to changes in the ocean forcing, and we show that the retreat becomes irreversible after 20 years of warm ocean conditions. A comparison to experiments with a simple depth-dependent melt rate parameterization demonstrates that such parameterizations are unable to capture the details of the retreat process, and they overestimate mass loss by more than 40% over a 50 year timescale.

1. Introduction

In the recent history of Pine Island Glacier (PIG), it is thought that increased basal melting has thinned the ice shelf, leading to the present-day imbalance of the glacier and its sustained grounding line retreat with a rate close to 1 km a^{-1} [*Rignot*, 1998; *Joughin et al.*, 2010; *Park et al.*, 2013; *Rignot et al.*, 2014]. The onset of retreat predates the loss of a pinning point in the 1970s, as the glacier receded from a 400 m high subglacial ridge oriented transverse to the prevailing ice flow direction [*Jenkins et al.*, 2010]. The rapid retreat of PIG illustrates how the grounding line of marine terminating glaciers can change at subdecadal timescales, a process which has been observed for many other glaciers in both Antarctica, e.g., *Rott et al.* [2002] and *Rack and Rott* [2004], and the Arctic, e.g., *Rosenau et al.* [2013]. Model simulations for the future evolution of PIG have suggested that the retreat slows down when a new stable or temporarily stable grounding line location is reached [*Joughin et al.*, 2010; *Favier et al.*, 2014; *Cornford et al.*, 2015]. Such pinning points for the grounding line include, but are not limited to, topographic features of the underlying bedrock, such as locally elevated areas. Other factors play an equally important role for grounding line stability, such as basal slipperiness, side drag, and ice shelf buttressing, both on a downward or retrograde bed slope [*Gudmundsson et al.*, 2012]. As observations about the bed in the vicinity of the grounding line are difficult to obtain, a detailed description of grounding-line conditions in Antarctica and elsewhere remains unavailable. However, we cannot rule out the possibility that a substantial fraction of marine-terminating glaciers have a geometrical high at their grounding zone.

In a world where many marine-terminating glaciers are undergoing grounding-line retreat, often forced by changes in ambient ocean conditions, it is important to understand the basic topographic controls imposed by the presence of a bedrock ridge on the grounding-line dynamics during such retreat. An important role is played by the basal mass balance of the ice shelf, which has a direct effect on the ice shelf thickness, and hence, the amount of back pressure transferred to the upstream grounded ice [*Thomas*, 1979]. For the Pine Island Ice Shelf, results from ocean instruments at the ice front and below the ice shelf in conjunction with phase sensitive ice-penetrating radar on the ice shelf and ocean-modeling work [*Thoma et al.*, 2008; *Stanton et al.*, 2013; *Dutrieux et al.*, 2014] have indicated a strong temporal variability in basal melt rates from subannual to interannual timescales, in response to a variable amount of ocean heat transported to the ice base. In addition, previous ocean-modeling work based on a series of idealized ice shelf cavity shapes and discarding ice-ocean

feedbacks has shown that sub-ice shelf melt rates can increase rapidly as a glacier thins and retreats from a subglacial bedrock ridge on which it was previously grounded [*De Rydt et al.*, 2014]. PIG is a prime candidate for this process.

While a community effort is underway to represent melt rates and patterns underneath Antarctica's ice shelves better [*Asay-Davis et al.*, 2015], most current-day ice dynamics models still use a simplified melt rate parameterization, often represented by a piecewise linear function of the ice draft [*Joughin et al.*, 2010; *Pollard and DeConto*, 2012; *Favier et al.*, 2014; *Joughin et al.*, 2014] or a function of the slope of the ice base [*Little et al.*, 2012]. A more physically based approach was adopted by *Parizek and Walker* [2010], *Gladish et al.* [2012], *Walker et al.* [2013], and *Sergienko* [2013], who coupled the ice dynamics equations to a plume model to describe the buoyancy-driven meltwater circulation underneath the ice shelf [*Holland and Feltham*, 2006], allowing the study of feedback mechanisms between the ice and ocean. Yet none of these parameterizations account for the full three-dimensional ocean dynamics; in particular, they discard the important topographical steering of ocean currents in the presence of a nontrivial bathymetry. This relatively unexplored link between the ocean circulation and sub-ice shelf melt rates has potentially large consequences for the ice dynamics during glacier retreat, and it remains to be demonstrated how regularly used ice dynamics models with a simplified and computationally cheap melt rate parameterization perform in comparison to computationally more expensive approaches that use a full three-dimensional ocean circulation model to compute the melt rates. Moreover, the studies that have used plume theory to compute basal melt rates do not include grounding-line dynamics, hence neglecting potentially important feedbacks between ocean melting and ice motion.

In this work we present the first results from a coupled ice-ocean model that simulates the retreat of an *idealized* glacier from a subglacial ridge, inspired by the ongoing retreat of PIG. We use a state-of-the art ice dynamics model, Úa, with grounding-line resolving capabilities [*Gudmundsson et al.*, 2012; *Pattyn et al.*, 2013; *Gudmundsson*, 2013], supplemented by a three-dimensional ocean circulation model, MITgcm [*Marshall et al.*, 1997; *Losch*, 2008]. Our approach is similar to the one proposed by *Goldberg et al.* [2012a] and *Goldberg et al.* [2012b] and is based on the exchange of model output between Úa and MITgcm at fixed time intervals. This is a so-called offline or asynchronous coupling method. At each coupling time step, the ice shelf geometry is transferred to MITgcm, which is spun up to a new steady state, and values for the updated ice shelf fresh water flux are used by Úa to advance the ice geometry until the next coupling time step. We show that results for this approach converge in the limit of a small coupling time step, and the method is optimized to simulate the inherent feedbacks between cavity geometry, basal melt rates, and grounding-line motion that occur at timescales longer than the coupling time step.

The experimental design of this paper are as follows. (i) For a synthetic PIG-like bedrock topography with a subglacial ridge transverse to the ice flow direction, the coupled model is stepped forward in time, using a cold far-field ocean forcing with a deep thermocline, taken from conductivity-temperature-depth (CTD) data in Pine Island Bay in 2012 [*Dutrieux et al.*, 2014]. A steady state geometry with stable grounding-line position on the ridge crest is established, which is assumed to be representative for PIG prior to its present day retreat. (ii) The coupled steady state is subsequently perturbed by applying a step change to warm ocean conditions with a shallow thermocline, as observed in Pine Island Bay in 2009 [*Jenkins et al.*, 2010]. The warm forcing is sustained for periods between 15 and 50 years to allow the glacier to retreat from the subglacial ridge and to study the reversibility of this process. Results reveal a previously unknown mechanism of grounding-line retreat and associated large changes in subglacial melt rates and provide physical constraints on the reversibility of the grounding-line retreat. (iii) In the final part, all experiments are repeated but using two straightforward depth-dependent melt rate parameterizations ("cold" and "warm") taken from the literature. New insights are obtained into the limitations of these simple melt parameterizations, and a comparison with the coupled ice-ocean approach provides a number of conclusions about the benefits and shortcomings of each method.

2. The Ice Shelf Without Subglacial Melting

2.1. Ice Dynamics: Model Setup and Domain Geometry

All ice dynamics simulations are carried out using the numerical model Úa [*Gudmundsson et al.*, 2012; *Gudmundsson*, 2013; *Pattyn et al.*, 2013; *Favier et al.*, 2014], which solves the dynamical equations in the shallow ice stream approximation (SSTREAM or SSA) [see, e.g., *Hutter*, 1983]. The bedrock geometry, B, is similar to the one used in *De Rydt et al.* [2014] and is an idealized representation of the central, fast-flowing section of PIG, with a deep trough and steep valley sidewalls, and a bathymetric ridge perpendicular to the ice flow

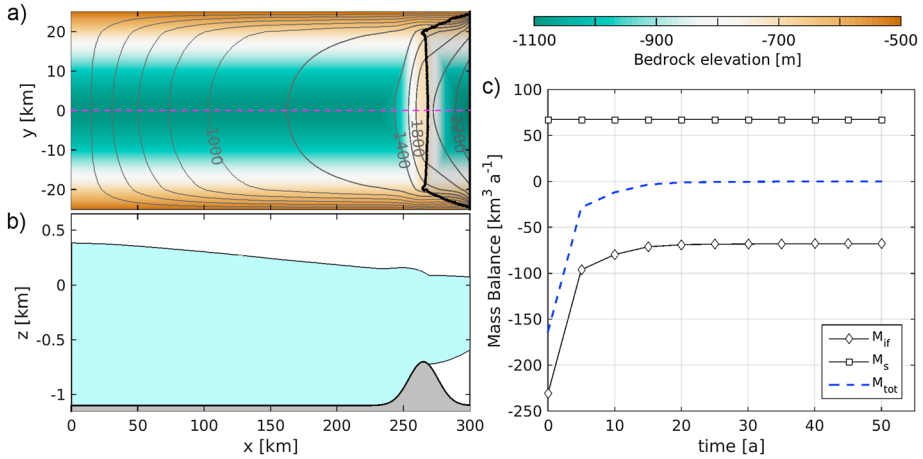

Figure 1. Properties of the model domain and control experiment. (a) Green-to-brown colors show the bedrock geometry as specified in equation (1) with a 400 m high ridge at $x = 265$ km. Contour lines correspond to the surface velocities in units of m a^{-1}. The black line indicates the position of the grounding line. (b) A section of the bedrock topography and steady state ice thickness along the centerline (magenta line in Figure 1a). (c) Evolution of the surface mass balance (M_s), flux through the ice front (M_{if}), and total mass balance (M_{tot}) as the ice stream-ice shelf configuration is stepped forward toward a steady state. The basal melt component is zero in the control experiment and therefore not shown.

direction that rises 400 m above the surrounding valley floor [*Jenkins et al.*, 2010]. A plan view of the bedrock is shown in color in Figure 1a: A 50 km-wide and 1100 m-deep valley stretches from the ice divide at $x = 0$ km where the ice velocities are set to zero, to the ice front, which is kept fixed at $x = 300$ km. The valley is uniform in the x direction and has a sinusoidal shape in the y direction,

$$B(x, y) = -\left(500 + 600 \sin\left(\frac{\pi y}{5 \times 10^4} + \frac{\pi}{2}\right)\right), \tag{1}$$

in units of meter. Superimposed on this channel is a transverse bedrock ridge with a maximum elevation at $x = 265$ km. The ridge has a Gaussian profile in the x direction, with a spread of $\sigma_b = 1.1 \times 10^4$ km,

$$\Delta B(x, y) = -1100 + 400 \exp\left(-\frac{(x - 2.65 \times 10^5)^2}{2\sigma_b^2}\right). \tag{2}$$

A longitudinal cross section of the bedrock geometry at $y = 0$ km is shown in Figure 1b.

The ice rheology is described by Glen's law with flow exponent $n = 3$ and a constant rate factor $A = 2.94 \times 10^{-9}$ a^{-1} kPa^{-3} corresponding to ice of −20°C according to *Cuffey and Paterson* [2010]. In order to represent better the observed narrow shear margins of PIG, a 5 km wide zone of softer ice is assumed along the lateral margins, where A is set to 5.04×10^{-9} a^{-1} kPa^{-3} (−10°C according to *Cuffey and Paterson* [2010]). At the lateral boundaries ($y = -25$ km and $y = 25$ km) a zero-flow constraint is imposed. Bedrock sliding is described by a nonlinear Weertman type sliding law with sliding exponent $m = 3$ and a constant sliding coefficient $C = 20$ m a^{-1} kPa^{-3}.

The surface mass balance is chosen such that the total surface accumulation over the model domain is comparable to the total amount for the PIG catchment, obtained from measurements (67.3 ± 6.1 Gt a^{-1} [*Medley et al.*, 2014]) and mass balance models (63.3 Gt a^{-1}, RACMO2 [*Lenaerts et al.*, 2012]). The surface accumulation in the model varies linearly from $a_s = 15$ m a^{-1} at the ice divide ($x = 0$ km) to $a_s = 1$ m a^{-1} at $x = 150$ km and is set to a constant value $a_s = 1$ m a^{-1} between $x = 150$ km and the ice front at $x = 300$ km. As a result, the glacier-wide surface mass balance is $M_s = \int a_s = 67.5$ Gt a^{-1}.

Úa employs finite element methods on an unstructured mesh with time-dependent mesh refinement around the grounding line. For this particular set of experiments, quadratic six-node triangular elements are used. For the bulk of our experiments, the distance between element vertices varies from ∼1.5 km for the upper catchment and interior of the ice shelf to < 300 m in the vicinity of the grounding line, with a mean element size of about 600 m. The fine resolution allows for a robust and accurate description of the

grounding-line movement and the mechanical coupling between the grounded ice and floating ice shelf [*Pattyn et al.*, 2013]. In comparison with previous studies [*Gudmundsson et al.*, 2012; *Gudmundsson*, 2013; *Pattyn et al.*, 2013; *Favier et al.*, 2014; *De Rydt et al.*, 2015], Úa uses a fully coupled time-stepping algorithm, where in each time step one solves simultaneously for changes in ice thickness, velocity, and grounding-line position, using a consistent streamline-upwind Petrov-Galerkin stabilization.

2.2. Control Case: Results Without Sub-Ice Shelf Melting

The model is stepped forward in time until a steady state geometry is obtained for the ice stream and ice shelf. In this particular case, *no basal melt* is applied to the ice shelf, and the final steady state is henceforth referred to as the 'control state'. The results after $t = 50$ years of spin-up time are summarized in Figure 1.

In Figure 1a, the ice flows from left to right, with the ice divide at $x = 0$ km. The ice thickness, depicted by the contour lines in Figure 1a, varies from $h \sim$1500 m at the divide to $h \sim$700 m at the ice front. In the central part of the domain, the grounding line runs parallel to the subglacial ridge at $x \approx 268.5$ km, i.e., 3.5 km downstream of the ridge crest and cuts across contours of constant ice thickness near the lateral boundaries. A section of the bathymetry and ice thickness along the center line of the glacier (dashed magenta line in Figure 1a) is shown in Figure 1b. The bathymetric ridge causes a surface expression upstream of the ridge, and the ice becomes afloat downstream of the ridge crest. In the absence of subglacial melting, the draft of the ice shelf has a convex shape.

Modeled surface velocities (contours in Figure 1a) vary from $u_s = 0$ m a^{-1} at the divide and along the lateral margins, to $u_s \approx 2200$ m a^{-1} at the center of the ice front. Values near the grounding line are $u_s \approx 1900$ m a^{-1} in the central part of the ice stream and sharply decrease toward the lateral boundaries across a 5 km wide shear margin.

Figure 1c depicts the evolution of the mass balance components and total mass balance, as the model is spun up toward a steady state. All mass balance components are integrated over the entire model domain. The total mass balance is the sum of the basal mass balance M_b (negative for melting), surface mass balance M_s (positive for accumulation), and ice flux through the ice front M_{if} (negative for outflow):

$$M_{\text{tot}} = M_b + M_s + M_{\text{if}}\,. \tag{3}$$

In this case, $M_b = 0$ Gt yr^{-1}, and for a system in balance, $M_{\text{tot}} = 0$ Gt yr^{-1}. After roughly 50 years, the system reaches a balanced configuration, with the outflow at the ice front balancing the accumulation at the surface.

The control case provides the starting point for all further experiments.

3. Coupled Ice-Ocean Modeling

Ice shelf melt rates are provided to Úa through the offline coupling with a stand-alone three-dimensional ocean circulation model, MITgcm [*Marshall et al.*, 1997]. At every coupling time step, Δt_c, MITgcm computes the new steady state ocean circulation for the current ice shelf geometry and returns an updated melt rate field to Úa. The assumption of a steady state entails that at every coupling time step, MITgcm is spun up from a uniformly stratified ocean until temporal changes to the stratification, circulation, and melt rates are the result of numerical noise. A steady state is typically reached after 2 months, although a more conservative spin-up time of 6 months is used in all simulations. The melt rates are averaged over the final 2 weeks of the ocean simulation, before being transferred to Úa.

As the offline coupling method assumes that the ocean is in steady state at any given time for the prescribed boundary forcing, a recomputation of the melt rates is required for every time step in Úa, which is typically on the order of 15 days. However, the ice shelf geometry does not substantially change at this timescale and neither do the melt rates. The coupling time step Δt_c can therefore be increased without appreciably changing the results, while reducing the computation time required for MITgcm. The point at which the melt rates and geometry start to diverge with increasing Δt_c will be tested in section 4.2, and it suffices to say here that Δt_c is set to 1 year in all further experiments.

3.1. The Ocean Model Setup

The MITgcm, which is used here in its hydrostatic configuration, has been modified to include the pressure loading and thermodynamic forcing of a steady ice shelf [*Losch*, 2008], and subsequent minor modifications

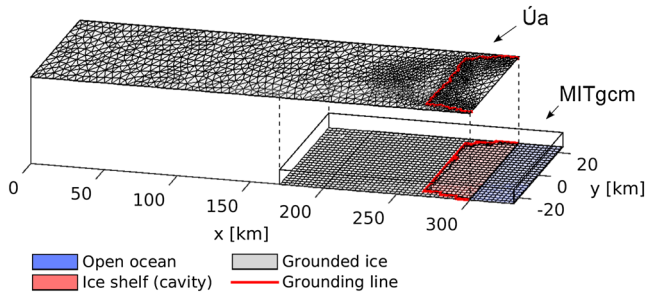

Figure 2. Ice and ocean model domains. Úa uses finite element methods on an unstructured grid with finest resolution near the grounding line (red line) and in areas that are close to floatation. MITgcm is a finite volume code on a structured grid and with a static representation of the ice shelf cavity. The grids depicted here are for illustration purposes only and do not reflect the exact resolution of our experiments.

have been made to optimize the melt rate computation, such as the use of average values of temperature, salinity, and frictional velocity over a 20 m thick boundary layer [*De Rydt et al.*, 2014]. As a z coordinate model with partial-cell treatment of the topography, the MITgcm allows an accurate description of the cavity geometry. Our model grid consists of 55 layers with a vertical spacing of 20 m and a structured horizontal grid with an eddy-resolving resolution of 625 m. The model domain is shown in Figure 2 and covers the area downstream of $x = 170$ km to allow for a growing ice shelf cavity, supplemented by an additional 30 km of open ocean. The grids shown in Figure 2 are for illustration purposes only and do not reflect the resolution of the real model grid. More information about specific model details can be found in *De Rydt et al.* [2014], including a description of the conservation equations for heat and salt fluxes at the ice-ocean interface, and vertical mixing and advection schemes.

3.2. Grid Interpolations

The grid structure and resolution of Úa and MITgcm are different, and mapping of variables from one grid to the other is done using a simple linear interpolation method. As the mesh in Úa is generally finer than the ocean grid, in particular near the grounding line, the interpolation of the ice shelf cavity geometry onto the MITgcm grid does not introduce any appreciable errors. On the other hand, the interpolation of the melt rate from the coarser MITgcm mesh onto the Úa grid effectively leads to a spatial smoothing of the melt rate pattern, without loss of information.

Typically, z coordinate circulation models such as the MITgcm require the application of a minimum water-column thickness, as a minimum of two vertical grid cells is required in order to resolve any overturning circulation. We impose a minimum water-column thickness of 40 m or two vertical grid cells by deepening the bedrock topography in areas where the ice draft approaches the bathymetry. This typically occurs in a small region close to the grounding line, where the ice base and bedrock surface converge. This method guarantees a precise representation of the slope of the ice base and an accurate simulation of the slope-driven meltwater plume and melt rates. Alternative methods to impose the minimum water-column thickness were tested, such as carving away a fraction of the bedrock and/or the ice. However, such methods were found to produce spurious temporal oscillations in the melt rates.

3.3. Hydrographic Forcing

Melt rates are computed within the MITgcm for a prescribed set of ocean boundary conditions. In general, these include the atmospheric forcing at the surface and hydrographic forcing at the open edges of the model domain. We neglect the surface forcing by imposing zero fluxes and impose constant temperature and salinity conditions at the open boundary at $x = 330$ km. The values are restored over a 3 km-wide margin (five horizontal grid cells), with a restoring timescale which varies from 6 h at the boundary to 12 h in the interior. We use two different temperature and salinity profiles, denoted by (T_{600}, S_{600}) and (T_{800},S_{800}), which are depicted by the dashed and solid lines in Figure 3. The subscripts for T and S refer to the bottom depth of the thermocline and halocline, respectively.

The imposed profiles closely follow the hydrographic conditions observed in Pine Island Bay [*Jacobs et al.*, 1996], with a cold (−1°C) and fresh (34) layer of Winter Water close to the surface freezing temperature overlaying a layer of warm (1.2°C) and saline (34.7) Circumpolar Deep Water with a temperature up to 4°C above

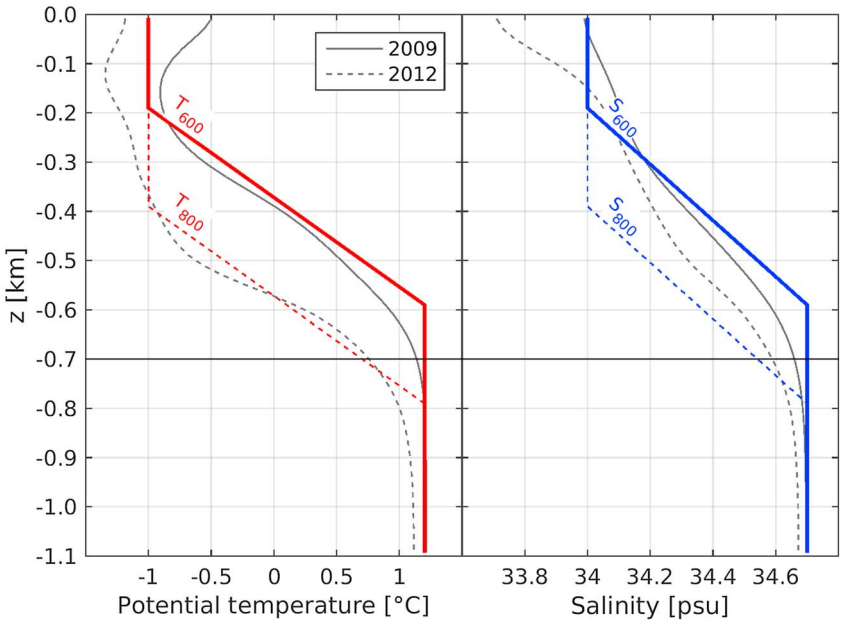

Figure 3. Restoring conditions for temperature and salinity at the open boundary of the model domain. The warm conditions (T_{600}, S_{600}) have a thermocline and halocline that extend down to 600 m and closely follow observations of T and S in Pine Island Bay in 2009 (solid black line) [*Jacobs et al.*, 2011]. The cold conditions (T_{800}, S_{800}) have a deeper thermocline and halocline and approximately correspond to observations of T and S in 2012 (dashed black line) [*Dutrieux et al.*, 2014].

the in situ freezing point. The two water masses are joined by a thermocline and halocline with linearly varying temperature and salinity.

A record of hydrographic conditions in Pine Island Bay during the austral summers of 1994, 2007, 2009, 2010 and 2012 show that the depth of the thermocline and halocline vary considerably at interannual timescales [*Jacobs et al.*, 2011; *Dutrieux et al.*, 2014]. The warmest year on record is 2009, with a thermocline extending down to a depth of about 600 m. The piecewise linear profiles (T_{600}, S_{600}) closely follow the averaged temperature and salinity sections obtained from 89 CTD casts taken in the austral summer of 2009 in Pine Island Bay [*Jacobs et al.*, 2011] (solid black lines in Figure 3). The coldest year on record is 2012, with the thermocline extending down to a depth of about 800 m, and the profiles (T_{800}, S_{800}) closely follow the average 2012 observations (dashed black lines in Figure 3).

4. Evolution of Pine Island Glacier Using a Coupled Ice-Ocean Model

4.1. Cold Ocean Forcing: A New Steady State

Starting from the control state in section 2, which did not include basal ablation, we simulate the evolution of the ice shelf geometry and glacier dynamics subjected to ocean-driven melting. Cold conditions (T_{800}, S_{800}) are imposed at the ocean boundary, and the coupled model is stepped forward in time for 50 years with a coupling time step of 1 year. At the start of the simulation, melt rates range from $-10\,\mathrm{m\,a^{-1}}$ to about $-50\,\mathrm{m\,a^{-1}}$. The 50 year evolution of the spatially integrated mass balance components and total mass balance are shown in Figure 4. At time $t = 0$, when basal melting is turned on ($M_b < 0$), the total mass balance M_{tot} becomes negative. Over time, the system readjusts to the imposed ice shelf melting, which leads to a decrease in mass flux through the ice front, while the basal mass balance stays approximately constant. As a result, the total mass balance asymptotically tends to zero, and the ocean and ice reach a mutual equilibrium with a stable grounding line position after about 50 years.

A summary of the new steady state geometry and ocean conditions at $t = 50$ years is given in Figure 5. Figure 5a shows the new ice thickness (colors), surface speed (contours), and grounding-line position (black line). Compared with the control state, the ice shelf has thinned, slowed down, and retreated. The new ice shelf thickness is asymmetrical transverse to the prevailing ice-flow direction, with the thinnest ice found along the left shear margin at $y = 25$ km. A similar result was previously obtained by *Goldberg et al.* [2012a].

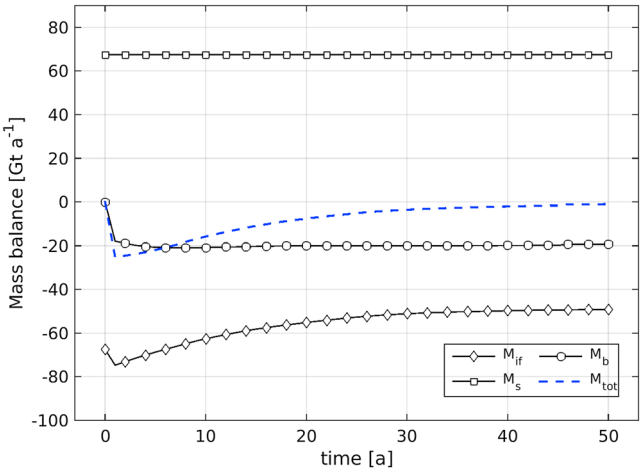

Figure 4. Evolution of the mass balance components during a 50 year coupled ice-ocean experiment with cold forcing at the ocean boundary, stepped forward from the control state geometry with a coupling time step $\Delta t_c = 1$ year. The basal mass balance M_b remains approximately constant after the initial time step, whereas the ice flux through the ice front M_{if} reduces by about 40%. The total mass balance M_{tot} tends to zero, and the simulation approaches a steady state.

Areas of thin ice coincide with regions of high melt rate caused by the entrainment of warm water into the buoyant meltwater plume and turbulent mixing of heat toward the ice base; see Figure 5b. The plume originates toward the margin at $y = -25$ km, and as the meltwater fraction increases along its path, the added buoyancy leads to an increase in momentum, with speeds up to 0.3 m s^{-1}. Geostrophic balance steers the plume toward the left and parallel to contours of constant ice thickness. Eventually, it gets deflected by the bedrock wall at $y = 25$ km, where it forms a boundary current that flows out toward the open ocean. This clockwise rotation of the buoyancy-driven meltwater plume is a common large-scale feature of the circulation underneath idealized Antarctic ice shelves, see, e.g., *Grosfeld et al.* [1997]. Despite the asymmetry in the melt pattern and ice thickness, the grounding line and surface velocity are approximately symmetrical with respect to the centerline.

A section along the centerline of the glacier further highlights ice shelf thinning (Figure 5c) and the transmission of this thinning upstream of the grounding line. The ice shelf draft at the ice front coincides with the top of the thermocline, whereas the warmest and densest water is found below the top of the ridge and is

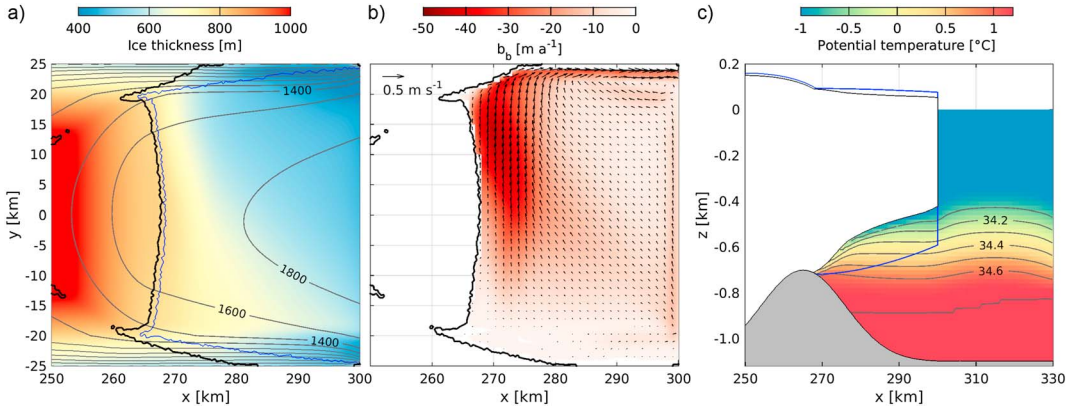

Figure 5. Properties of the final steady state after 50 years of coupled ice-ocean spin-up time with cold ocean restoring conditions (T_{800}, S_{800}). (a) Colors show ice thickness, and contour lines represent surface speed. The black line corresponds to the new grounding line location, and the blue line is the position of the control state. (b) Ice shelf melt rates are shown in red, and arrows correspond to the ocean current at the ice base for every second grid cell, averaged over the top 20 m of the water column. (c) A section of bedrock and ice shelf geometry along the centerline of the glacier shows thinning compared with the control case (blue outline). Colors and contours represent the ocean potential temperature and salinity, respectively.

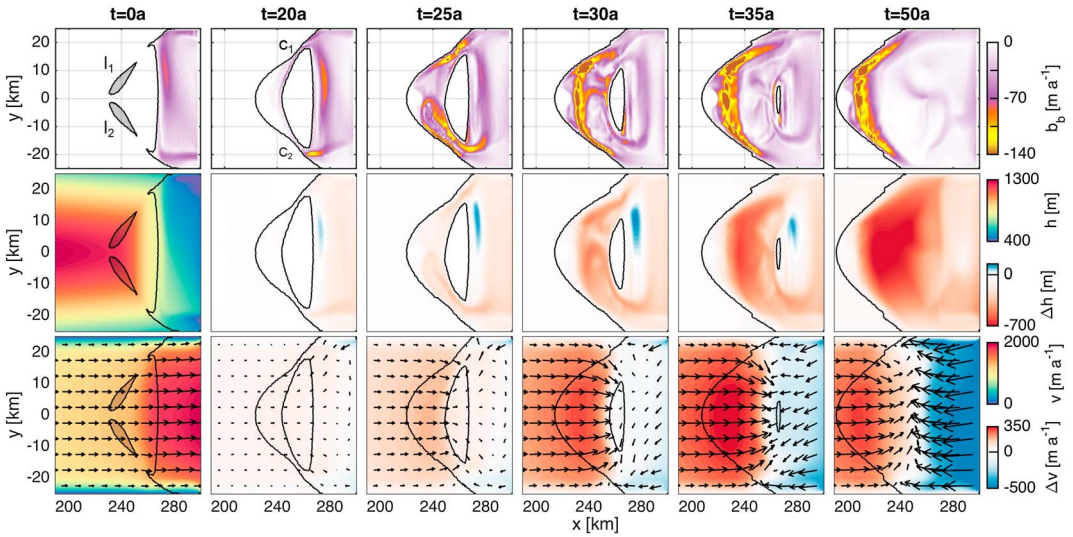

Figure 6. (top row) A time series of melt rates, (middle row) changes in ice thickness, (bottom row) and changes in surface velocity, as the glacier retreats from the subglacial ridge at $x = 265$ km in response to warm ocean conditions (T_{600}, S_{600}). Changes in ice thickness h, surface speed v, and surface velocity components $\vec{v}$ for $t > 0$ are computed with respect to the values at $t = 0$, shown in the first column. In the top left, l_1 and l_2 identify the location of two isolated lakes that form upstream of the grounding line. They eventually merge with the main ocean cavity via two channels, indicated by c_1 and c_2 in the adjacent figure. The black line indicates the position of the grounding line.

therefore not in contact with the bottom of the ice shelf. This explains the relatively low melt rates, up to -50 m a^{-1}, compared with present-day observations which exceed -100 m a^{-1} near the grounding line [*Dutrieux et al.*, 2013].

4.2. Warm Ocean Forcing: Pine Island Glacier Retreat

Increased warm water transport onto the continental shelf and the circulation of surplus heat toward the coastline has been associated with ice shelf thinning and grounding-line retreat around the margins of West Antarctica [*Shepherd et al.*, 2004; *Jacobs et al.*, 2011; *Dutrieux et al.*, 2014] and Greenland [*Holland et al.*, 2008; *Straneo and Heimbach*, 2013; *Inall et al.*, 2014]. To simulate these effects for the idealized version of PIG, the steady state obtained for cold ocean conditions and described in the preceding section is perturbed by raising the thermocline and halocline of the far field ocean forcing, which leads to an instantaneous increase in the heat delivered to the ice base. In this experiment, the ocean boundary condition (T_{600}, S_{600}) has a thicker layer of modified Circumpolar Deep Water, which extends 100 m above the 700 m high ridge crest. The warm water is in direct contact with the ice base in the vicinity of the grounding line, which leads to an instantaneous increase in basal melt by a factor of 2.5, with maximum melt rates exceeding -100 m a^{-1}.

In response to the increased basal melt, the ice shelf starts to thin and the grounding line retreats. Figure 6 shows the melt rates (top row), change in ice thickness (middle row), and the change in surface velocity and speed (bottom row) after 0, 20, 25, 30, 35, and 50 years. Two movies are included in supporting information that further illustrate the evolution of the glacier geometry (S1) and basal melt rates (S2) during the retreat. At the onset of retreat, ice shelf thinning and drawdown of grounded ice due to increased velocities across the grounding line leads to the growth of two isolated lakes (indicated by l_1 and l_2 and shaded in grey) upstream of the grounding line. These areas are marginally afloat, with a water column between the ice base and the bedrock of only a few meters, assuming that the local subglacial water pressure is equal to the ocean pressure at equal depth. As the water in these locations is disconnected from the main ocean cavity, no basal melt is applied. At around $t = 10$ years both lakes connect, and after $t = 15$ years they eventually merge with the main ice shelf cavity and become exposed to ocean melting (not shown). This leads to the formation of an ice rumple, i.e., a locally grounded area of the ice shelf, which slowly reduces in size and eventually ungrounds. Loss of buttressing due to ice shelf thinning and ungrounding from the stabilizing subglacial ridge leads to a speedup of the ice shelf upstream of the ridge ($x = 265$ km) by up to 350 m a^{-1}. Downstream of the ridge, a significant slowdown happens during the final 15 years of the simulation, as the ice adjusts to its new stress regime with a fully floating central section. This suggests that the shelf is too buttressed for the upstream increase in velocity to propagate further downstream.

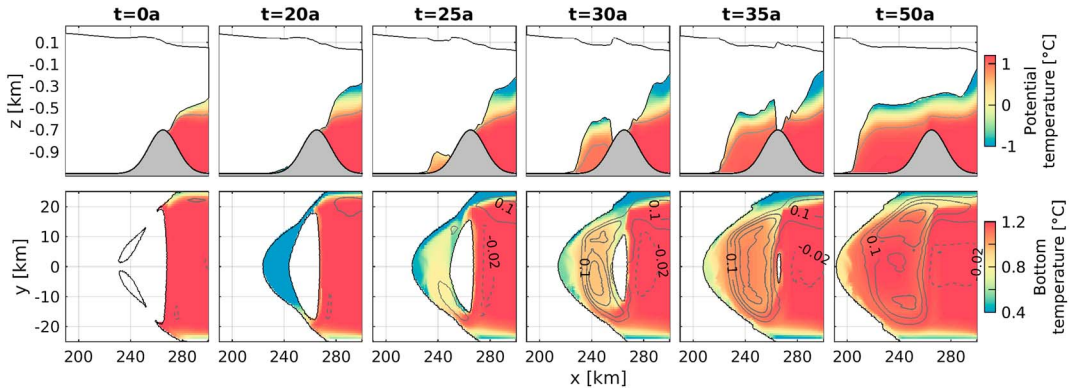

Figure 7. (top row) A cross section of ice shelf geometry and ocean temperature along the centerline, and (bottom row) ocean bottom temperature and contours of the depth-averaged barotropic stream function, as the glacier retreats from the subglacial ridge in response to warm ocean conditions (T_{600}, S_{600}). Note the difference in colorscale between rows. In the top row, the grey line corresponds to the 34.6 salinity contour. In the bottom row, the solid contour lines are 0.05 sverdrup (Sv, 106 m^3/s) apart and correspond to a cyclonic (clockwise) circulation; the dashed line is the −0.02 Sv contour and indicates an anticyclonic circulation.

From $t = 20$ years, the basal channels that connect the shallow upstream cavity with the main ocean cavity (indicated by c_1 and c_2 in Figure 6), expand in both height and width, allowing warm water to flow across the ridge and into the deep cavity. The critical factor that controls the inflow of warm water is the height of the channels at the ridge crest [*De Rydt et al.*, 2014]. Initially, the shallow connections only accommodate the outflowing meltwater plume, and a cold hydrographic front at the ridge crest prevents warm water from penetrating into the deep cavity. Once the gap between the ice base and the underlying bathymetry widens and exceeds 200 m, the cold meltwater plume separates from the bedrock, and warm bottom water is able to flow across the ridge. This process is illustrated in Figure 7, which shows a section of temperature and the 34.6 salinity contour along the centerline of the domain (top row), as well as snapshots of ocean bottom temperature and contours of the depth integrated barotropic stream function (bottom row). The circulation of warm water into the deep cavity increases over time and coincides with the formation of a cyclonic circulation inland of the ridge and a jet along the inland side of the ridge with a strength up to 0.3 m s^{-1}. The pattern of the ocean circulation and temperature distribution are dictated by the presence of the subglacial ridge and correspond well to observations and realistic simulations of oceanographic conditions underneath the present-day ice shelf of PIG [*Dutrieux et al.*, 2014].

The increase in ocean heat delivered to the ice base and the emerging barotropic circulation are directly related to the change in ice shelf geometry, in particular the erosion of the cavity upstream of the ridge. The feedback between ocean circulation and cavity geometry in turn has an important effect on the melt rate: Figure 8a shows that between $t = 20$ years and $t = 35$ years, the total melt water production increases more than threefold from about 40 Gt a^{-1} at the onset of cavity formation to about 130 Gt a^{-1} when the base of the ice shelf disconnects from the ridge top. The increase in total freshwater production cannot be explained by the exposure of newly ungrounded ice to ocean melting, as the ice shelf area only increases by 60% between $t = 20$ years and $t = 35$ years.

The results in Figure 8a are shown for three different coupling time steps: 0.5 years, 1 year, and 5 years. For $\Delta t_c = 0.5$ years and $\Delta t_c = 1$ year, meltwater fluxes do not significantly deviate, whereas there is a noticeable difference between results for $\Delta t_c = 1$ year and $\Delta t_c = 5$ years. We conclude that for a coupling time step of 1 year, results have converged and are robust.

If we interpret the x position of the furthest upstream ocean grid node, denoted by x_{GL}, as a simplified measure for the grounding-line location, then the temporal evolution of x_{GL} allows us to distinguish between four phases of glacier retreat, shown in Figure 8b. Phase I coincides with a slow retreat of the grounding line at a rate of about 0.3 km a^{-1} and ends after $t = 10$ years when the cavity upstream of the ridge connects to the ocean, indicated by a jump in the grounding-line location from $x = 258$ km to $x = 226$ km. During phase II, the meltwater flux remains constant (Figure 8a) while the channels c_1 and c_2 grow as a result of ice shelf thinning. At $t = 20$ years, the start of phase III is signaled by a rapid increase in meltwater volume and an acceleration of the grounding-line migration, as warm ocean water starts to circulate through the channels

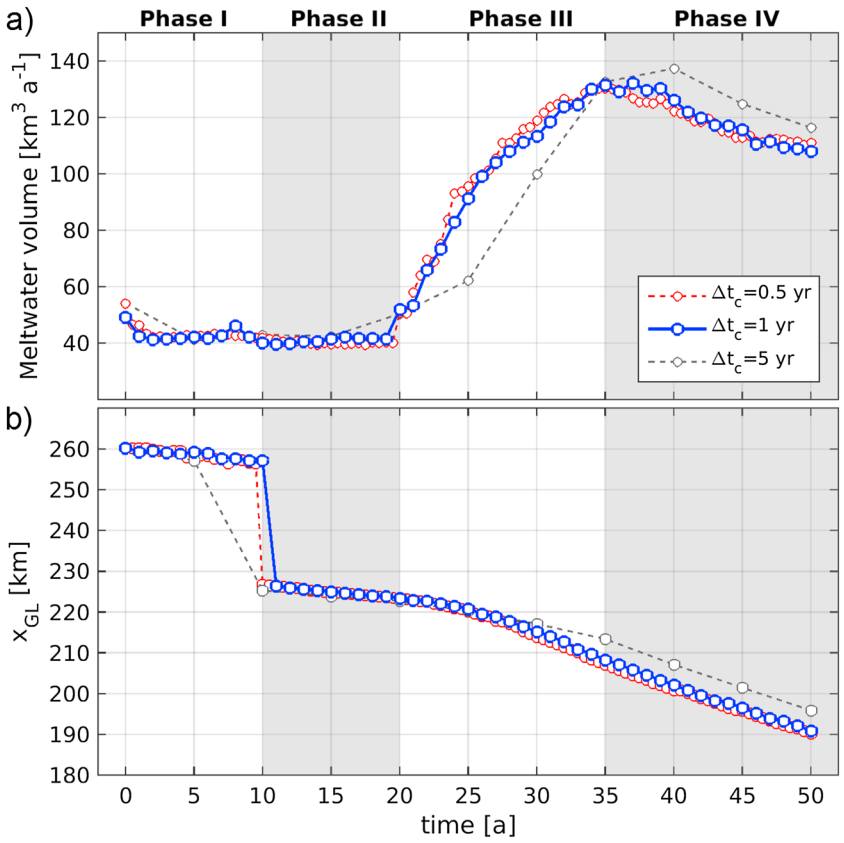

Figure 8. Evolution of (a) melt water volume and (b) grounding line position x_{GL} as the glacier retreats from a subglacial ridge in response to warm hydrographic forcing at the open ocean boundary. Values are shown for three different coupling time steps: $\Delta t_c = 0.5$ year, $\Delta t_c = 1$ year, and $\Delta t_c = 5$ years. Four different phases of grounding line retreat can be distinguished, which are discussed in section 4.2.

and across the ridge. After 35 years, the ungrounding from the ridge is complete and the final phase IV is characterized by a steady retreat of the glacier at a rate of about 1.1 km a1 and a slow linear decrease in melt rates of about 2 Gt a^{-2} as the ice shelf further thins and the ice base rises up into shallower, colder water. The retreat is indefinite, and no new steady state is reached within the model domain inland of the ridge.

4.3. Reversibility of Grounding Line Retreat

An interesting question remains whether the ocean-driven retreat of PIG from its subglacial pinning point and the associated formation of the deep cavity is a reversible process. In particular, does a decline in available heat after a period of warm ocean conditions cause the grounding line to readvance? We find that in the limiting case where the basal melt reduces to zero, the glacier will always readvance and reestablish its grounding-line position on the ridge, irrespective of how far it has retreated under warm ocean conditions. However, a more realistic experiment consists of a return to cold, preretreat values of the ocean forcing, with a deep thermocline at 800 m and associated low melt rates. We study three different scenarios, all of which exhibit an initial period of warm ocean conditions (T_{600}, S_{600}) and grounding line retreat, followed by a step change back to cold conditions (T_{800}, S_{800}). The change in the forcing occurs after 15 years (Scenario 1), 25 years (Scenario 2), or 35 years (Scenario 3), and each simulation is run for a total of 50 years. The grounding-line migration for each experiment is shown in Figure 9.

In Scenario 1, warm ocean conditions are applied for 15 years before reverting back to cold ocean conditions. The grounding line location remains stable at around $x = 225$ km for more than 20 years, after which the cavity inland of the ridge closes off from the open ocean and the grounding line readvances to its preperturbed location on the ridge crest ($x \approx 260$ km). For ungrounded parts of the ice shelf that are isolated from the main ocean cavity, melt rates are set to zero, whereas the remainder of the ice shelf produces a total meltwater volume that relaxes back to 20 Gt a^{-1} (not shown), as previously obtained in section 4.1 for the cold steady state scenario.

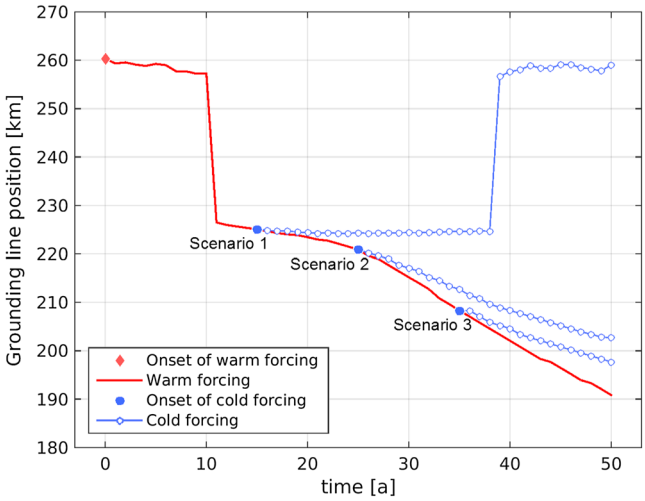

Figure 9. Grounding line migration for warm ocean conditions (red line) and three perturbation scenarios in which the hydrographic forcing is switched back to cold conditions after 15 years (Scenario 1), 25 years (Scenario 2), and 35 years (Scenario 3).

In Scenarios 2 and 3, warm ocean conditions are applied for 25 and 35 years respectively, before reverting back to cold ocean conditions. The grounding line continues to retreat after the onset of cold ocean conditions, despite a 45% reduction in the melt rates and thickening of the ice shelf. The initial retreat rate is 650 m a^{-1} in both scenarios, with a gradual slowdown to 600 m a^{-1} at around 50 years. This is about 450 m a^{-1} slower than the retreat driven by warm ocean forcing, shown by the red line in Figure 9. These results suggest that for our particular choice of model forcing and geometry, any period of sustained warm ocean conditions between 15 and 25 years pushes the idealized representation of PIG into a phase of irreversible grounding-line retreat.

The discontinuity in grounding-line response, which occurs between 15 and 25 years, coincides with the start of phase III of retreat, shown in Figure 8. Before this time, the majority of ice shelf melting occurs seaward of the subglacial ridge and a lowering of the thermocline leads to a sufficient reduction in melt rates for the channels c_1 and c_2 to close and the grounding line to readvance onto the ridge. On the other hand, if a return to cold conditions occurs after the start of phase III, the channels c_1 and c_2 are large enough to sustain the inflow of water at intermediate depth into the deep cavity and cause a sufficient amount of melting inland of the ridge to maintain grounding-line retreat. This is true despite the fact that for cold hydrographic conditions (T_{800}, S_{800}), the bottom of the thermocline is situated 100 m below the ridge crest, and the warm modified Circumpolar Deep Water is not able to circulate across the ridge toward the ice base.

5. Comparison With Results From a Simple Melt Rate Parameterization

Our use of a three-dimensional ocean circulation model to compute ice shelf melt rates as input for an ice dynamics model is not unique [*Determann et al.*, 2012; *Gladstone et al.*, 2012; *Goldberg et al.*, 2012a, 2012b; *Thoma et al.*, 2015; *Asay-Davis et al.*, 2015], though most other studies in the literature use a variety of melt rate parameterizations that account for the regional differences in ocean temperature and the dependence of melt rates on ocean circulation in a simplified way. The most frequently used parameterizations assume a monotonically increasing function of the melt rate with depth, see, for example, *Joughin et al.* [2010], *Martin et al.* [2011], *Pollard and DeConto* [2012], and *Favier et al.* [2014]. Other studies have investigated the dependence of melt rates on the local geometry of the ice shelf, such as its slope [*Little et al.*, 2009; *Jenkins*, 2011; *Little et al.*, 2012]. These simplified relationships do not incorporate the important interactions between ocean circulation and basal melt for PIG, and a comparison with results from the coupled simulations provides an ideal opportunity to test their adequacy in a geometrically nontrivial setup.

5.1. Choice of Melt Rate Parameterizations

Figure 10a shows six melt rate scenarios which have previously been applied in model simulations to study the transient grounding-line motion of PIG with a realistic geometry. They are labeled m_{iF} with $i \in \{1, 2, 3, 4\}$ [*Favier et al.*, 2014], m_P [*Pollard and DeConto*, 2012], and m_J [*Joughin et al.*, 2010]. Each parameterization is a monotonically increasing function with depth, and although the spread between these functions is

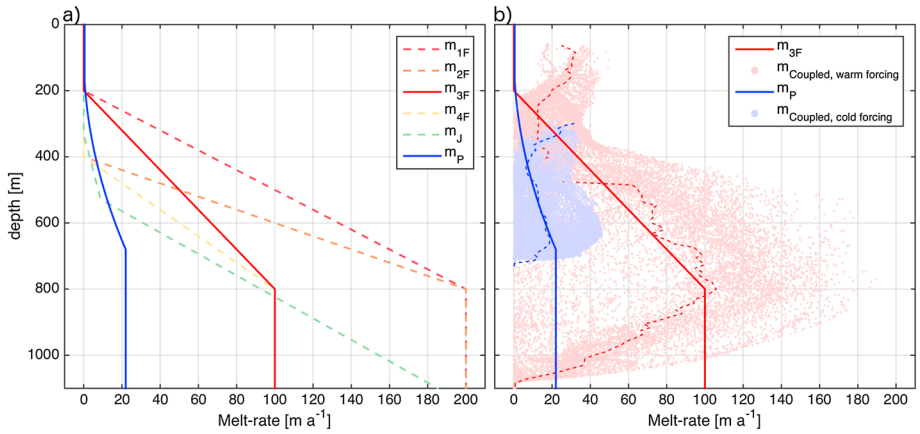

Figure 10. (a) Depth-dependent melt rate parameterization for six scenarios that have previously been used in the literature to predict future grounding line retreat of Pine Island Glacier. Four scenarios m_{1F}–m_{4F} are taken from *Favier et al.* [2014], m_J is taken from *Joughin et al.* [2010], and m_P is taken from *Pollard and DeConto* [2012]. (b) Scatter plot of melt rate versus depth for the coupled steady state with cold ocean forcing after 50 years (blue dots) and the coupled simulation with warm forcing after 50 years (red dots), as well as averages of the melt rate at any given depth (dashed blue and red lines). The solid blue and red lines correspond to m_P and m_{3F}, respectively, and provide the best fit to the melt distribution of the coupled simulations.

significant, their shape broadly reflects the thermal structure of ocean water in the Pine Island Embayment, and their magnitude is based on direct and indirect measurements of basal melt and its interannual variability [*Dutrieux et al.*, 2013; *Stanton et al.*, 2013; *Dutrieux et al.*, 2014].

Although the parameterizations are in broad qualitative and quantitative agreement with observations, their monotonicity assumes that melt rates are highest at the deepest point, i.e., directly at the grounding line. This assumption has been falsified by a number of ocean modeling studies that use plume theory to constrain basal melt processes, at least in the absence of subglacial runoff or tides; see, e.g., *Jenkins* [2011]. It is also apparent from our coupled ice-ocean results. Figure 10b shows a scatter plot of melt rates versus depth for the coupled steady state with cold ocean forcing after 50 years (section 4.1), and the coupled simulation with warm forcing after 50 years (section 4.2). In both cases, peak melt rates are found some distance away from the deepest point. In addition, simplified melt rate parameterizations do not reproduce the zonal distribution of melt imposed by the Coriolis-driven path of the meltwater plume or the impact of a nontrivial bathymetry on the ocean properties adjacent to the ice base, which leads to the large spread of melt rates in Figure 10b at any given depth, with a RMS error that generally exceeds 50%. On the other hand, the benefit of a fixed melt parameterization is a significant reduction in computational time by at least a factor of 5, as expensive ocean simulations are not required.

In order to compare both approaches, we select two parameterizations from Figure 10a that best reproduce the melt-depth relation from the coupled simulations with a cold and warm ocean forcing. For the cold case, the parameterization by *Pollard and DeConto* [2012] provides the best fit, whereas in the warm case, the third parameterization from *Favier et al.* [2014] approximately follows the averaged melt rates versus depth. Using these two choices, we perform the exact same sequence of simulations as in section 4. (i) Starting from the control state, the model is spun up to a new steady state using low melt rates (m_P) for a period of 50 years. (ii) Subsequently, the steady state is perturbed by a step function in the melt rates to higher values (m_{3F}), and the simulation is run for another 50 years.

5.2. Pine Island Glacier Retreat Using a Simple Melt Rate Parameterization

Figure 11 summarizes the results of the experiment by comparing the spatially integrated freshwater volume (a), ice volume loss (b), and grounding-line motion (c) to equivalent results from the coupled approach. During the first 50 years of the simulation, the parameterized melt m_P and the coupled simulation with cold forcing (T_{800}, S_{800}) both produce a constant fresh water flux around 20 km^3 a^{-1}. The loss of ice volume is somewhat smaller for the parameterized melt case due to a thicker shelf at the ice front, which leads to higher buttressing and a grounding line that reaches a stable position in a more advanced position.

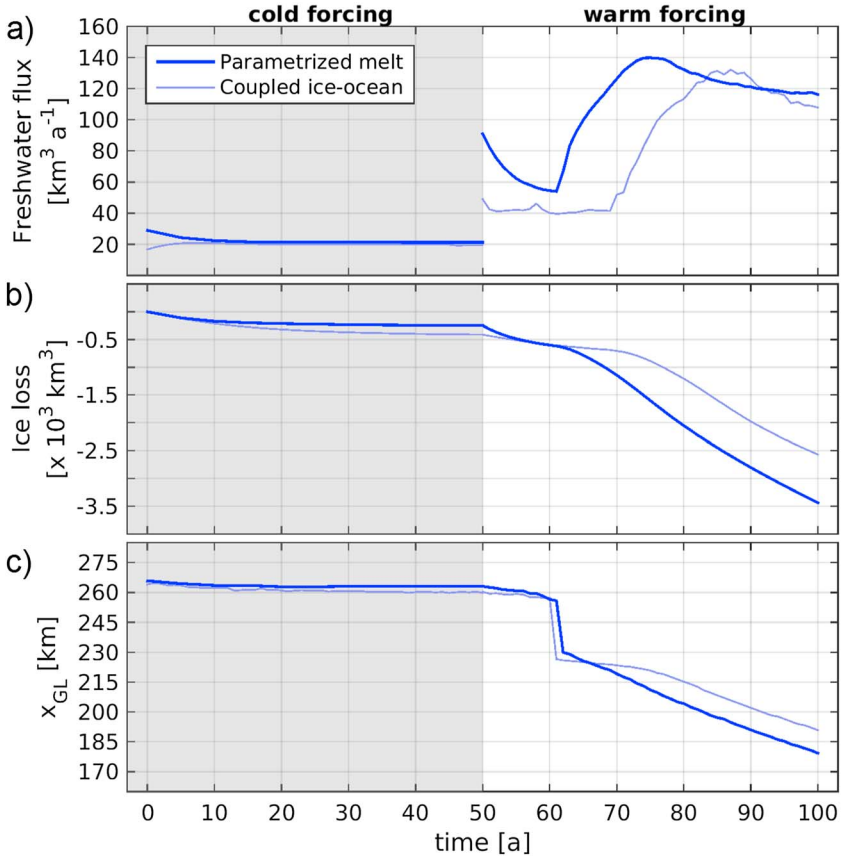

Figure 11. A comparison of the (a) spatially integrated melt rates, (b) ice volume loss, and (c) grounding line position x_{GL} for a coupled ice-ocean simulation and a simulation with parameterized melt rates. The forcing in the coupled experiment consists of cold ocean conditions (T_{800}, S_{800}) between $t = 0$a and $t = 50$a, and warm conditions (T_{600}, S_{600}) between $t = 50$a and $t = 100$a, identical to section 4.1 and section 4.2, respectively. The parameterized melt rates are m_P between $t = 0$a and $t = 50$a, and m_{3F} from $t = 50$a to $t = 100$a.

After 50 years,both simulations reach a steady state, with $x_{GL} = 260$ km for the coupled simulation and 3 km further downstream for the parameterized melt scenario.

At $t = 50$ years, the instantaneous change to higher melt rates m_{3F} leads to a step change in the meltwater flux from 20 km^3 a^{-1} to about 90 km^3 a^{-1}. The increase for the coupled model is much smaller, with a doubling of the flux. This discrepancy is caused by the high values of m_{3F} directly at the grounding line, whereas the meltwater plume in the coupled simulations produces more localized and smaller melt rates. Increased melting of the ice shelf leads to an imbalance of the mass budget in both approaches, and the grounding line starts to retreat at a rate of about 400 m a^{-1} for the parameterized case and 200 m a^{-1} for the coupled simulation. This period corresponds to phase I in Figure 8.

At $t = 62$ years, the upstream lakes l_1 and l_2 (see Figure 6) connect to the main ocean cavity, characterized by the jump in x_{GL}. For m_{3F} there is an instantaneous increase in meltwater volume flux, as the ice draft of the lakes is over 1000 m deep and the newly exposed ice shelf melts at a rate of −100 m a^{-1} everywhere. The grounding line starts to retreat faster, at a rate of 1.1 km a^{-1}. On the other hand, the response of the coupled simulation is very different. The grounding line continues to retreat slowly in response to near-to-constant melt rates, as the channels c_1 and c_2 are not large enough to allow warm water to circulate across the ridge and into the inner cavity. This physical process, which corresponds to phase II in Figure 8, is not reproduced by the parameterized melt scenario. Because phase II is absent, the ice-volume loss and grounding-line position start to diverge. At the end of the 100 year simulation, the grounding line in the parameterized melt case has retreated an extra 11.5 km as compared with the coupled experiment, and the glacier has lost an additional 896 km^3 or about 43% of its ice volume.

Despite these large differences, the results are qualitatively similar. For example, phase III, which is characterized by a rapid increase in meltwater production, exists between $t = 61$a and $t = 75$a for the parameterized melt rates and between $t = 70$a and $t = 85$a for the coupled simulation. Also during phase IV, melt rates slowly decrease while the grounding line continues to retreat at a similar rate of about 1.1 km a^{-1} in both approaches.

6. Discussion

Results show that if a thick layer of warm Circumpolar Deep Water is sustained at the ice front for longer than 15 years, the idealized glacier enters a phase of irreversible retreat. In reality, however, changes in forcing do not occur as a step function, and in the observational record at the ice front of PIG, the thermocline depth varies considerably at interannual and subannual timescales, without a clear periodicity [*Dutrieux et al.*, 2014]. Due to the absence of data before the 1990s, it is not known whether a sustained period of increased heat transport toward the PIG ice shelf has forced its present-day retreat or whether the average ocean forcing is slowly increasing with respect to a long-term (century-scale) climatology. The offline coupling could allow us to address the feasibility of the latter scenario, by imposing gradual (interannual) changes to the ocean forcing at timescales exceeding the coupling time step and the spin-up time required for the ocean model. It also allows us to test for the sensitivity and response of the system to a variety of ocean conditions different from the ones used in this study. Such tests are the topic of future research.

It is expected that feedback mechanisms which occur at short timescales, e.g., due to seasonality in ocean forcing or tidal effects, can only be resolved for a small coupling time step. Such short timescale feedback mechanisms have been ignored here, as we apply a temporally constant ocean forcing, and other feedbacks at subannual timescales, which are unrelated to the forcing, are found to be absent. Whereas the offline coupling assumes a steady state for the ocean, a fully coupled method that solves the ocean and ice dynamics equations as one system is particularly useful for studying such rapid changes in the ocean forcing. Due to small-scale variability in the melt rates, instabilities can develop, such as the formation of basal channels [*Gladish et al.*, 2012; *Sergienko*, 2013]. Such instabilities have not been observed in the results presented here, although we cannot exclude their existence for higher melt rate scenarios or weaker shear margins.

Ocean simulations with a static ice shelf geometry have suggested that the height of the seabed ridge relative to the bottom of the thermocline plays an important role in controlling the stability of the ice shelf, as it modulates the transport of warm water toward the grounding line [*De Rydt et al.*, 2014]. The prominent, 400 m high ridge underneath the PIG ice shelf might be unusual, yet smaller-scale features are likely to exist at all grounding lines. A broader analysis is required to test if the proposed mechanism of retreat, including the formation of an ice rumple, is robust for different amplitudes of the ridge, both in an idealized setup, and for realistic geometries which exhibit undulations at a range of wavelengths. In particular, a comparison to the limiting case of a flat bed is required to gain further insights into the role of a seabed ridge for the stability of tidewater glaciers.

Apart from the possible range of sensitivities to ocean and bathymetric conditions, results depend strongly on the choice of basal slipperiness and ice viscosity. In our setup, a 5 km wide band of softer ice was added to reproduce the observed shear margins of PIG. Yet the ice flow field depends on the strength of the shear margin, and possible shear weakening due to flow acceleration is not accounted for in the model. As a result, the timescales of the response to increased ocean heat and loss of buttressing due to ice shelf thinning are not independent of the choice of model parameters and should be treated with caution until further sensitivity tests are done. Better constraints on the basal slipperiness, ice viscosity, and their spatial and temporal variability can be obtained from model inversions which minimize the misfit between modeled and observed surface velocity and ice thickness, see, e.g., *Favier et al.* [2014] in the case of PIG.

To test the sensitivity of results to the model parameters and topography, simulations can be made easier and less computationally intensive if melt rates are adequately parameterized based directly on physical properties of the adjacent ocean and ice shelf geometry, hence making the use of offline or fully coupled model simulations less crucial. Although the depth-dependent melt rate parameterizations studied in section 5 produce qualitatively similar results to results from the coupled method, there is no evidence that the predicted rates of mass loss and grounding-line movement over a modest 50 year timescale are comparable. In particular, the chosen parameterizations overpredict melt rates near the grounding line, which leads to an additional mass loss of 43% over the simulation period. This large difference is unsatisfactory, in particular because the parameterizations were chosen to be an optimum fit to the melt rate distribution obtained from the coupled

model. In practise, such a fit is not possible as a priori knowledge about the coupled results is not available, and deviations for a "best guess" parameterization are expected to be even larger. Therefore, it is suggested that the shape of the depth-dependent melt rate parameterizations, which are frequently used in simulations of mass loss from the Antarctic Ice Sheet, are urgently reconsidered. For example, a correction for the "distance from the grounding line" based on plume theory can be incorporated, which is expected to render results more accurate, and at the same time less time consuming than a coupled approach.

7. Conclusions

Although this study is strongly motivated by the retreat of Pine Island Glacier from a seabed ridge, it addresses the more general question how changing ocean conditions affect the ice dynamics of ice streams and tidewater glaciers with a nontrivial subglacial topography at their grounding line. The processes involved are governed by complex feedback mechanisms between the ocean and ice dynamics, and they matter for all retreating glaciers in Antarctica and Greenland. We incorporate possible feedbacks through a relatively recent and novel approach in glaciology, which consists of an offline coupling between a shallow ice model and a three-dimensional ocean circulation model. The results from this coupled approach emphasize the important role of a seabed ridge in stabilizing the grounding line under cold ocean conditions and modulating the ocean currents, heat transport, and ice shelf melting once the ocean starts to warm and forces the grounding line to retreat. The two main conclusions of this study are as follows. A sustained period of warm ocean conditions exceeding 15 years forces the idealized representation of Pine Island Glacier to start its retreat from the subglacial ridge. The upstream migration of the grounding line becomes irreversible after about 20 years or as soon as a subglacial cavity forms inland of the ridge. Second, the simple melt rate parameterizations, which are regularly used in the literature to simulate the future evolution of the Antarctic ice volume, are unable to accurately represent the melt rate distribution or capture the complex feedbacks, leading to an overestimation of mass loss by at least 40% compared to the coupled approach.

Acknowledgments
J.D.R. was funded through a Marie Curie fellowship (European Union Seventh Framework Programme (FP7/2007-2013), grant PIEF-GA-2011-301268), and J.D.R. and G.H.G. were partly supported by core funding from the Natural Environment Research Council (NERC) to the British Antarctic Survey. We thank Adrian Jenkins, Paul Holland and two anonymous reviewers for their detailed comments that helped to improve the manuscript.

References

Asay-Davis, X., et al. (2015), Experimental design for three interrelated marine ice-sheet and ocean model intercomparison projects, *Geosci. Model Dev.*, *8*, 9859–9924.

Cornford, S. L., et al. (2015), Century-scale simulations of the response of the West Antarctic Ice Sheet to a warming climate, *The Cryosphere*, *9*, 1579–1600.

Cuffey, K. M., and W. S. B. Paterson (2010), *The Physics of Glaciers*, 4th ed., Butterworth-Heinemann, Oxford.

De Rydt, J., P. R. Holland, P. Dutrieux, and A. Jenkins (2014), Geometric and oceanographic controls on melting beneath Pine Island Glacier, *J. Geophys. Res. Oceans*, *119*, 2420–2438, doi:10.1002/2013JC009513.

De Rydt, J., G. H. Gudmundsson, H. Rott, and J. L. Bamber (2015), Modeling the instantaneous response of glaciers after the collapse of the Larsen B Ice Shelf, *Geophys. Res. Lett.*, *42*, 5355–5363.

Determann, J., M. Thoma, K. Grosfeld, and S. Massmann (2012), Impact of ice-shelf basal melting on inland ice-sheet thickness: A model study, *Ann. Glaciol.*, *53*, 129–135.

Dutrieux, P., D. G. Vaughan, H. F. J. Corr, A. Jenkins, P. R. Holland, I. Joughin, and A. H. Fleming (2013), Pine Island Glacier ice shelf melt distributed at kilometre scales, *The Cryosphere*, *7*, 1543–1555.

Dutrieux, P., J. De Rydt, A. Jenkins, P. R. Holland, H. K. Ha, S. H. Lee, E. J. Steig, Q. Ding, E. P. Abrahamsen, and M. Schrder (2014), Strong sensitivity of Pine Island ice-shelf melting to climatic variability, *Science*, *343*, 174–178.

Favier, L., G. Durand, S. Cornford, G. Gudmundsson, O. Gagliardini, F. Gillet-Chaulet, T. Zwinger, A. Payne, and A. Le Brocq (2014), Retreat of Pine Island Glacier controlled by marine ice-sheet instability, *Nat. Clim. Change*, *4*, 117–121.

Gladish, C. V., D. M. Holland, P. R. Holland, and S. F. Price (2012), Ice-shelf basal channels in a coupled ice/ocean model, *J. Glaciol.*, *58*, 1227–1244.

Gladstone, R. M., V. Lee, J. Rougier, A. J. Payne, H. Hellmer, A. L. Brocq, A. Shepherd, T. L. Edwards, J. Gregory, and S. L. Cornford (2012), Calibrated prediction of Pine Island Glacier retreat during the 21st and 22nd centuries with a coupled flowline model, *Earth Planet. Sci. Lett.*, *333–334*, 191–199.

Goldberg, D. N., C. M. Little, O. V. Sergienko, A. Gnanadesikan, R. Hallberg, and M. Oppenheimer (2012a), Investigation of land ice-ocean interaction with a fully coupled ice-ocean model: 1. Model description and behavior, *J. Geophys. Res.*, *117*, F02038, doi:10.1029/2011JF002247.

Goldberg, D. N., C. M. Little, O. V. Sergienko, A. Gnanadesikan, R. Hallberg, and M. Oppenheimer (2012b), Investigation of land ice-ocean interaction with a fully coupled ice-ocean model: 2. Sensitivity to external forcings, *J. Geophys. Res.*, *117*, F02038, doi:10.1029/2011JF002247.

Grosfeld, K., R. Gerdes, and J. Determann (1997), Thermohaline circulation and interaction between ice shelf cavities and the adjacent open ocean, *J. Geophys. Res.*, *102*, 15,595–15,610, doi:10.1029/97JC00891.

Gudmundsson, G. H. (2013), Ice-shelf buttressing and the stability of marine ice sheets, *The Cryosphere*, *7*, 647–655.

Gudmundsson, G. H., J. Krug, G. Durand, L. Favier, and O. Gagliardini (2012), The stability of grounding lines on retrograde slopes, *The Cryosphere*, *6*, 1497–1505.

Holland, D. M., R. H. Thomas, B. de Young, M. H. Ribergaard, and B. Lyberth (2008), Acceleration of Jakobshavn Isbrae triggered by warm subsurface ocean waters, *Nat. Geosci.*, *1*, 659–664.

Holland, P. R., and D. L. Feltham (2006), The effects of rotation and ice shelf topography on Frazil-Laden ice shelf water plumes, *J. Phys. Ocean.*, *36*, 2312–2327.

Hutter, K. (1983), *Theoretical Glaciology: Material Science of Ice and the Mechanics of Glaciers and Ice Sheets*, Springer, Netherlands.
Inall, M. E., T. Murray, F. R. Cottier, K. Scharrer, T. J. Boyd, K. J. Heywood, and S. L. Bevan (2014), Oceanic heat delivery via Kangerdlugssuaq Fjord to the south-east Greenland ice sheet, *J. Geophys. Res. Oceans*, *119*, 631–645, doi:10.1002/2013JC009295.
Jacobs, S. S., H. H. Hellmer, and A. Jenkins (1996), Antarctic Ice Sheet melting in the southeast Pacific, *Geophys. Res. Lett.*, *23*(9), 957–960, doi:10.1029/96GL00723.
Jacobs, S. S., A. Jenkins, C. F. Giulivi, and P. Dutrieux (2011), Stronger ocean circulation and increased melting under Pine Island Glacier ice shelf, *Nat. Geosci.*, *4*(8), 519–523.
Jenkins, A. (2011), Convection-driven melting near the grounding lines of ice shelves and tidewater glaciers, *J. Phys. Oceanogr.*, *41*, 2279–2294.
Jenkins, A., P. Dutrieux, S. S. Jacobs, S. D. McPhail, J. R. Perrett, A. T. Webb, and D. White (2010), Observations beneath Pine Island Glacier in West Antarctica and implications for its retreat, *Nat. Geosci.*, *3*(7), 468–472.
Joughin, I., B. E. Smith, and D. M. Holland (2010), Sensitivity of 21st century sea level to ocean-induced thinning of Pine Island Glacier, Antarctica, *Geophys. Res. Lett.*, *37*, L20502, doi:10.1029/2010GL044819.
Joughin, I., B. E. Smith, and B. Medley (2014), Marine ice sheet collapse potentially under way for the Thwaites Glacier Basin, West Antarctica, *Science*, *344*, 735–738.
Lenaerts, J. T. M., M. R. van den Broeke, W. J. van de Berg, E. van Meijgaard, and P. Kuipers Munneke (2012), A new, high-resolution surface mass balance map of Antarctica (1979–2010) based on regional atmospheric climate modeling, *Geophys. Res. Lett.*, *39*, L04501, doi:10.1029/2011GL050713.
Little, C. M., A. Gnanadesikan, and M. Oppenheimer (2009), How ice shelf morphology controls basal melting, *J. Geophys. Res.*, *114*, C12007, doi:10.1029/2008JC005197.
Little, C. M., D. Goldberg, A. Gnanadesikan, and M. Oppenheimer (2012), On the coupled response to ice-shelf basal melting, *J. Glaciol.*, *58*(208), 203–215.
Losch, M. (2008), Modeling ice shelf cavities in a *z* coordinate ocean general circulation model, *J. Geophys. Res.*, *113*, C08043, doi:10.1029/2007JC004368.
Marshall, J., C. Hill, L. Perelman, and A. Adcroft (1997), Hydrostatic, quasi-hydrostatic, and nonhydrostatic ocean modeling, *J. Geophys. Res.*, *102*, 5733–5752.
Martin, M. A., R. Winkelmann, M. Haseloff, T. Albrecht, E. Bueler, C. Khroulev, and A. Levermann (2011), The Potsdam Parallel Ice Sheet Model (PISM-PIK) Part 2: Dynamic equilibrium simulation of the Antarctic ice sheet, *The Cryosphere*, *5*, 727–740.
Medley, B., et al. (2014), Constraining the recent mass balance of Pine Island and Thwaites glaciers, West Antarctica, with airborne observations of snow accumulation, *The Cryosphere*, *8*(4), 1375–1392.
Parizek, B. R., and R. T. Walker (2010), Implications of initial conditions and ice–ocean coupling for grounding-line evolution, *Earth Planet. Sci. Lett.*, *300*(34), 351–358.
Park, J. W., N. Gourmelen, A. Shepherd, S. W. Kim, D. G. Vaughan, and D. J. Wingham (2013), Sustained retreat of the Pine Island Glacier, *Geophys. Res. Lett.*, *40*(10), 2137–2142.
Pattyn, F., et al. (2013), Grounding-line migration in plan-view marine ice-sheet models: Results of the ice2sea MISMIP3d intercomparison, *J. Glaciol.*, *59*(215), 410–422.
Pollard, D., and R. M. DeConto (2012), Description of a hybrid ice sheet-shelf model, and application to Antarctica, *Geosci. Model Dev.*, *5*(5), 1273–1295.
Rack, W., and H. Rott (2004), Pattern of retreat and disintegration of the Larsen B ice shelf, Antarctic Peninsula, *Ann. Glaciol.*, *39*(1), 505–510.
Rignot, E., J. Mouginot, M. Morlighem, H. Seroussi, and B. Scheuchl (2014), Widespread, rapid grounding line retreat of Pine Island, Thwaites, Smith, and Kohler glaciers, West Antarctica, from 1992 to 2011, *Geophys. Res. Lett.*, *41*, 3502–3509, doi:10.1002/2014GL060140.
Rignot, E. J. (1998), Fast recession of a West Antarctic glacier, *Science*, *281*(5376), 549–551.
Rosenau, R., E. Schwalbe, H.-G. Maas, M. Baessler, and R. Dietrich (2013), Grounding line migration and high-resolution calving dynamics of Jakobshavn Isbr, West Greenland, *J. Geophys. Res. Earth Surf.*, *118*, 382–395.
Rott, H., W. Rack, P. Skvarca, and H. De Angelis (2002), Northern Larsen Ice Shelf, Antarctica: Further retreat after collapse, *Ann. Glaciol.*, *34*(1), 277–282.
Sergienko, O. V. (2013), Basal channels on ice shelves, *J. Geophys. Res. Earth Surface*, *118*, 1342–1355, doi:10.1002/jgrf.20105.
Shepherd, A., D. Wingham, and E. Rignot (2004), Warm ocean is eroding West Antarctic Ice Sheet, *Geophys. Res. Lett.*, *31*, L23402, doi:10.1029/2004GL021106.
Stanton, T. P., W. J. Shaw, M. Truffer, H. F. J. Corr, L. E. Peters, K. L. Riverman, R. Bindschadler, D. M. Holland, and S. Anandakrishnan (2013), Channelized ice melting in the ocean boundary layer beneath Pine Island Glacier, Antarctica, *Science*, *341*(6151), 1236–1239.
Straneo, F., and P. Heimbach (2013), North Atlantic warming and the retreat of Greenland's outlet glaciers, *Nature*, *504*(7478), 36–43.
Thoma, M., A. Jenkins, D. Holland, and S. Jacobs (2008), Modelling Circumpolar Deep Water intrusions on the Amundsen Sea continental shelf, Antarctica, *Geophys. Res. Lett.*, *35*, L18602, doi:10.1029/2008GL034939.
Thoma, M., J. Determann, K. Grosfeld, S. Goeller, and H. Hellmer (2015), Future sea-level rise due to projected ocean warming beneath the Filchner Ronne Ice Shelf: A coupled model study, *Earth and Planet. Sci. Lett.*, *431*, 217–224.
Thomas, R. H. (1979), The dynamics of marine ice sheets, *J. Glaciol.*, *24*(90), 167–177.
Walker, R. T., D. M. Holland, B. R. Parizek, R. B. Alley, S. M. J. Nowicki, and A. Jenkins (2013), Efficient flowline simulations of ice-shelf/ocean interactions: Sensitivity studies with a fully coupled model, *J. Phys. Oceanogr.*, *43*, 2200–2210.